A Review of a B-spline based Volumetric Representation: Design, Analysis and Fabrication of Porous and/or Heterogeneous Geometries

Gershon Elber
Computer Science Department, Technion, Haifa 32000, Israel
Email: gershon@cs.technion.ac.il

June 30, 2023

Abstract

The needs of modern (additive) manufacturing (AM) technologies can no longer be satisfied by geometric modeling tools that are based on boundary representations (B-reps) - AM requires the representation and manipulation of interior heterogeneous fields and materials. Further, while the need for a tight coupling between design and analysis has been recognized as crucial almost since geometric modeling (GM) was conceived, contemporary GM systems only offer a loose link between the two, if at all.

For more than half a century, the (trimmed) Non-Uniform Rational B-spline (NURBs) surface representation has been the B-rep of choice for virtually all the GM industry. Fundamentally, B-rep GM has evolved little during this period. In this work, we review almost a decade of research and development in extending this boundary representation to a B-spline based, volumetric representation (V-rep) that successfully confronts the existing and anticipated design, analysis, and manufacturing foreseen challenges. We have extended all fundamental B-rep GM operations, such as primitive and surface constructors, and Boolean operations, to trimmed trivariate V-reps. This enables the much-needed tight link between the designed geometry and (iso-geometric) analysis on one hand and the full support of (additive) manufacturing of porous, (graded-) heterogeneous and anisotropic geometries, on the other. Examples and applications of V-rep GM, that span design, analysis and optimization, and AM, of lattice- and micro-structure synthesis as well as graded-heterogeneity, are demonstrated, with emphasis on AM.

Keywords: lattices and microstructures, functionally graded material, additive manufacturing, functional tiles

1 Introduction

The spline based boundary representation (B-rep) has been introduced to the geometric modeling community over fifty years ago. Nowadays, all commercial geometric computer aided design systems

employ this spline based B-rep as their representation of choice. B-reps were the right solution when the manufacturing process was subtractive. That is, a computer numerically controlled (CNC) cutter that removed material from a stock of aluminum or steel. In other words, the initial stock was homogeneous to begin with and so was the final carved artifact. Having homogeneous and isotropic geometries, there was no need for representing interior properties.

In fact, this lack of need to represent the interior was never true with respect to analysis. Spline based B-reps have been typically converted to piecewise linear volumetric finite elements (FE), like tetra and hexa, in order to analyze these geometries, a conversion process (to FE, but also back into the spline model!) that, in many cases, is more difficult than the analysis itself [10]. Clearly, the physical properties of any geometry are governed by the interior of the model and not just by its boundaries. Further, results of such analyses typically yield heterogeneous fields inside the geometry, such as stress or heat flex, which cannot be represented using B-reps. Finally, because analysis results typically affect the design, this design-and-analysis cycle is, in many cases, repeated multiple times. It is not surprising then that a tight connection between the design's geometric representation and the analysis representation has been recognized as highly desired, almost since GM was conceived.

About two decades ago, iso-geometric analysis [29, 10] (IGA) was introduced as an analysis paradigm, in an aim to overcome the large gap between the representations of the design and analysis stages. The use of a unified representation was preached, and specifically, the spline representation that is common in all modern GM systems, namely (trimmed) B-spline/Non Uniform Rational B-spline (NURBs) based geometry, has also been used in analysis, directly and with no representation conversion.

Modern additive manufacturing allows for the fabrications of models with functionally graded materials as well as porosity. Both (graded) heterogeneity and porosity are properties of the interior of a model and, again, are not representable with ease, if at all, using B-reps. In fact, we are in a first-ever situation where the manufacturing capabilities, as offered by modern 3D printers, are ahead of our GM tools.

For the last decade or so, we have been developing a GM kernel [27] that is based on a volumetric representation (V-rep). The proposed V-rep is based on (trimmed) trivariate B-spline/NURBs functions, where a trivariate is a function of three variables or volumetric. The benefits we gain by employing this representation include:

- Being a volumetric representation, the representation of graded heterogeneity on one hand, and of general fields such as stress or heat flux on the other hand, are fully supported.

- These fields, being part of the geometric trivariate representation, can precisely match desired boundary conditions. Further, the boundaries of the V-reps are merely trimmed surfaces. In other words, the boundaries of V-reps are fully compatible with the existing B-reps of all contemporary GM systems.

- Using symbolic computation, directly in the B-spline function spaces, we are able to build lattices [1] that are precisely conforming to a general freeform shape, and no tile is being clipped. Based on external prescriptions, for example from the end user or following analysis results,

[1] in this work, we employ the terms lattice and microstructure interchangeably to denote the same - a spatial porous structure, typically as a 3D topological grid of tiles, whereas a tile is a 3D volumetric element in the 3D grid, that others might denote as a cell.

the geometry, the topology, and the graded material contents of individual tiles can be fully adjusted and controlled.

- A unified representation for both design and analysis. Our (trimmed) trivariates are immediately usable in IGA, as will be briefly demonstrated here, with all the additional potential benefits in having higher order finite elements, with, possibly, higher continuity.

The rest of this work is organized as follows. In Section 2, we consider related work on and with trivariate splines whereas in Section 3, we introduce our B-spline trivariate based V-reps. Section 4 examines the algorithms needed to bring V-reps all the way to 3D printing and Section 5 exemplifies these abilities on additional examples. Finally, we conclude in Section 6.

2 Related Work

In this Section, we only discuss previous work that is related to volumetric splines. Clearly other volumetric representations exist, most notably the discrete voxel based representation, but this and similar representations are beyond the scope of this effort.

In the computer graphics community, trivariate splines were employed, for example, to thicken stick figures of general topologies [36], where the challenge has been to construct proper volumetric joints of general, n-sided, arms. Earlier, in [40], the well known idea of freeform deformation (FFD) was introduced where geometry was mapped through a Bézier trivariate volume. Quite a few variants of FFDs were introduced over the years. See, for example [19] and [26].

The use of trivariate B-spline functions is not new. Pierre Bézier introduced "Bézier cubes" in [4], toward volumetric morphing, a result that predated the FFD work of [40] by almost a decade. Bézier also employed trivariate Béziers in car design while multivariate splines (parametric splines with arbitrary number of parameters) were discussed in the 60s [20]. That said, most if not all FFDs are discrete approximations of the precise conforming lattices we introduce in this review, using functional composition [14, 12].

In [31], harmonic functions are employed to build and parameterize volumetric trivariate B-spline functions. In [41], a hybrid scheme is employed, in an effort to convert a trimmed surface based B-rep model to a V-rep model. Aiming at a watertight representation, that is a challenge to any GM system that employs trimming, a hybrid volumetric model is constructed, that preserves the original (trimmed) B-rep boundaries. In [13], different volumetric splines are discussed, such as (truncated) hierarchical B-splines, T-splines and LR B-splines, and compared.

In [38], scalar trivariate B-splines were used toward sculpting freeform shapes in 3D. Trivariates can represent surfaces in motion. In [9, 28], trivariate functions are employed to represent the swept volume of a parametric surface along a 3D path. The envelope of the trivariate is reduced to and computed as a zero set of the Jacobian of a trivariate. Zeros of trivariates (and multivariates) were also extensively used to solve quite a few problems in geometric modeling, such as the computation of offset curves and (trimmed) surfaces, bisectors and trisectors, flecnodal and offset curves over surfaces, packing and intersection problems, and in general, problems that can be reduced into a set of multivariate algebraic constraints [21, 2, 42]. Toward this end, a B-spline based multivariate solver has been developed and employed, exploiting favorable properties of splines, namely the convex hull containment and subdivision properties. This multivariate solver has also been employed toward AM in [18], to solve heterogeneous slicing problems, as will be discussed later in this review.

In the IGA community, the need for a volumetric representation was also recognized. See, for example [1]. A recent work of [37] sought the construction of trivariate splines from B-Rep NURBs, to be used in 3-space IGA. Typically, in IGA, Bézier patches, including trivariates, are extracted from the B-spline or NURBs geometry, in a process denoted as *Bézier extraction* [5], only to serve as the finite elements.

While, as was demonstrated, trivariate splines have been studied to a great extent, it was never aimed to be employed as a representation of choice in a GM kernel. Even today, the numeric instabilities that all modern GM system have to face in light of the trimmed surface based B-reps, are not negligible. Yet, in this review, we present an extension of trimmed B-spline based B-reps to trimmed trivariate B-spline based V-reps and show that the expected benefits are high, if a V-rep based kernel is to be used. This, while the numerical (Boolean operations) challenges in V-reps are almost the same as in B-reps, and can further be based on B-rep solutions.

3 The B-spline based Volumetric Representation

We now briefly discuss the fundamentals behind our trimmed trivariate based V-reps. A trivariate B-spline $\mathcal{T}$ is typically a mapping from a (u, v, w) box domain $D \subset \mathbb{R}^3$ to $\mathbb{R}^k$, $k \geq 3$, for the three XYZ spatial dimensions, but possibly also for additional dimensions of graded materials, properties, and fields:

$$\begin{aligned} &\mathcal{T}(u, v, w) \\ &\quad = \sum_{i=0}^{l} \sum_{j=0}^{m} \sum_{k=0}^{n} P_{ijk} B_i^{o_u}(u) B_j^{o_v}(v) B_k^{o_w}(w), \end{aligned} \tag{1}$$

where $\mathcal{T}$ is a trivariate with a control mesh of size $(l+1, m+1, n+1)$, control points $P_{ijk} \in \mathbb{R}^k$, and B-spline basis functions B^{o_q} of orders o_q, $q \in \{u, v, w\}$.

In the rest of this section, we will briefly exemplify, in Section 3.1, how trivariate primitives and volumetric constructors can be formed, and how Boolean operations can be computed, in Section 3.2. Then, in Section 3.3, some discussion of symbolic operations on trivariates will be presented and specifically functional composition toward geometry conforming lattice constructions.

3.1 Trivariate Primitives and Constructors

We start the discussion on V-reps by presenting ways to construct simple shapes as trivariate V-reps. Figure 1 presents two examples of primitive V-reps - a sphere and a truncated cone. The sphere consists of seven different trivariates - one trilinear cube at the center and six additional ruled trivariates between a face of the central cube and a corresponding spherical cap (see [8]), of orders $(5 \times 5 \times 2)$. The truncated cone consists of five trivariate, again one central trilinear pyramid and four trivariates on the cone's boundaries, of orders $(3 \times 2 \times 2)$. In all, we support the construction of the following trivariate primitives: a box, a skewed box, a sphere, a cylinder, a cone, a truncated cone and a torus. All primitives but the sphere are of quadratic degree at the most, if rational, and also, optionally, approximated as cubic piecewise polynomial B-splines.

One can also construct these primitives using a single singular trivariate, or a trivariate that contains sub-regions where the Jacobian vanish. While we also support the construction of such sin-

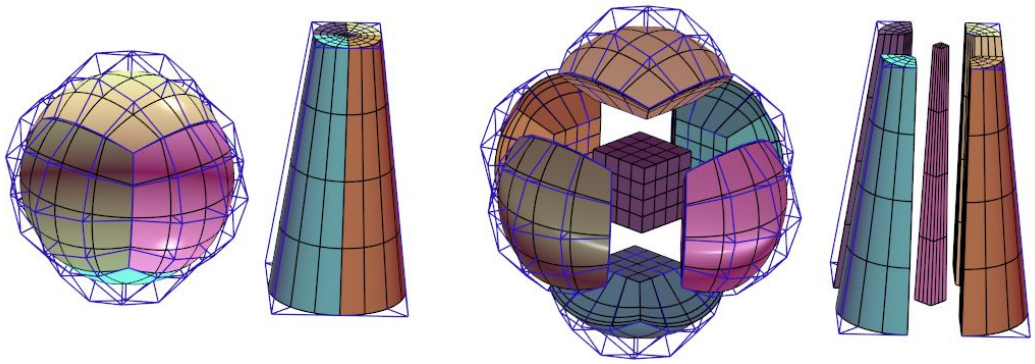

Figure 1: Two trivariate primitives - a sphere and a cone. Left shows regular views whereas exploded views are shown on the right. Every trivariate is painted in a different color, iso parametric curves are drawn in black and the control meshes of the different trivariates are drawn in blue.

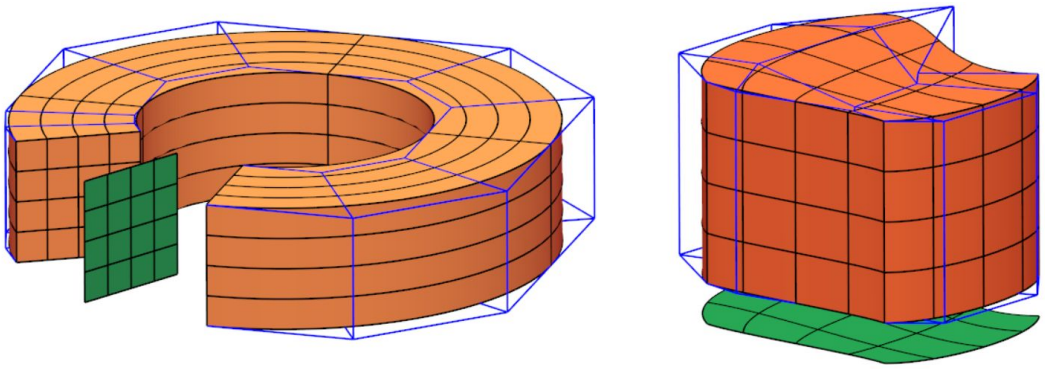

Figure 2: Two examples of constructed V-reps, as a trivariate of revolution on the left and extruded trivariate on the right. Iso parametric curves are drawn in black and the control meshes of the trivariates are drawn in blue.

gular trivariates, singular trivariates are detrimental in analysis and, here, we offer these alternatives of more trivariates per primitive that are all regular, or their Jacobian never vanish.

In Figure 2, two constructed trivariates are shown. On the left a volume of revolution is presented, rotating a surface to yield a trivariate and on the right a surface is extruded out of the plane, into a trivariate. In all, the construction as trivariates of extruded volume, ruled volume, volume of revolution, swept volume, and volumetric Boolean Sum [17] are supported.

In addition, many special operations on trivariate B-splines are also supported, operations that are required in further geometry processing, including analysis and manufacturing. Those include, for example, evaluations (positions and derivatives), subdivision and refinement, region extraction, interpolation and fitting, partial derivatives at specific locations and as fields, point inclusion and projection queries, slicing and intersections, etc. See [33] for more, on the topics discussed in this section.

3.2 Boolean operations in V-reps

The computation of Boolean operations (union, intersection, and subtraction) over geometry has always been a major challenge in GM systems. This, when the governing representation has been B-rep based trimmed B-spline/NURB surfaces.

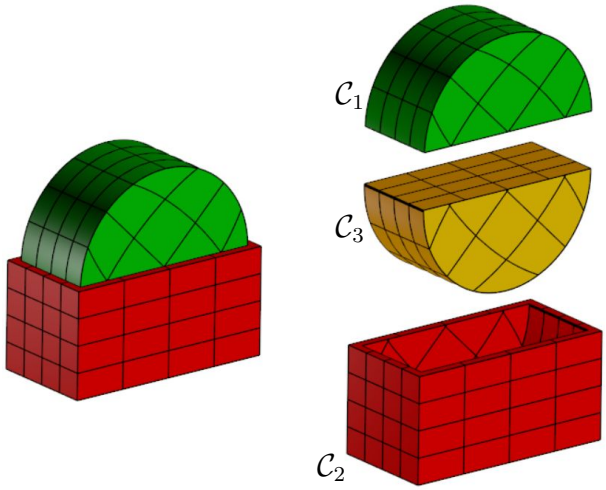

Figure 3: On the left, the union between a red (material) V-rep box and a green (material) V-rep cylinder is shown. The right shows an exploded view of the three VCells that are formed here.

A V-rep model, or a *VModel* for short, is defined as an extended, 3-manifold volumetric, representation of the half-edge data structure [30], typically used to represent 2-manifold graphs, herein, vertices, edges, and faces. The VModel will consist of several *VCells*, each of which is a (potentially trimmed) trivariate. A VCell is bounded by trimming surfaces, whereas the trimming surfaces themselves are trimmed by trimming curves.

Figure 3 demonstrates this. Shown is the union of a red box and a green cylinder, where different colors depict different materials. This union Boolean operation results in three VCells. While VCells $\mathcal{C}_1$ and $\mathcal{C}_2$ retain their original color, a question emerges what will be the color of $\mathcal{C}_3$, and should it be homogeneous or heterogeneous? See [33] for more on V-rep Boolean operations.

In all, the representation is volumetric and hence, one can appreciate the added complexity in Boolean operations for V-rep over B-rep. Luckily, we can divide the problem into two - considering the boundaries and the interior as almost two independent problems:

1. Boolean operations over the boundaries of the V-rep input model. These 2-manifold problems are reduced to traditional Boolean operations in B-reps and hence, one can exploit existing B-rep kernels to compute the boundaries of the result, from the boundaries of the input V-reps, that are regular trimmed B-spline based B-rep geometries.

2. The interior of the V-rep model is introducing a new challenge - an optional necessity to blend as-smoothly-as-needed interior properties and fields (recall $\mathcal{C}_3$ in Figure 3). Here, we offer a blending scheme that is based on the distances to boundaries of the different input V-reps, in the VCell, and their material content.

To exemplify the material blending scheme we employ, in the interior of VModels, see Figure 4. The figure presents a cross section of the simple example of a union of a red box and a green cylinder from Figure 3. Again, three VCells are formed here:

1. VCell $\mathcal{C}_1$ as the region of the cylinder out of the box that stays with green material.

2. VCell $\mathcal{C}_2$ as the region of the box out of the cylinder that stays with red material.

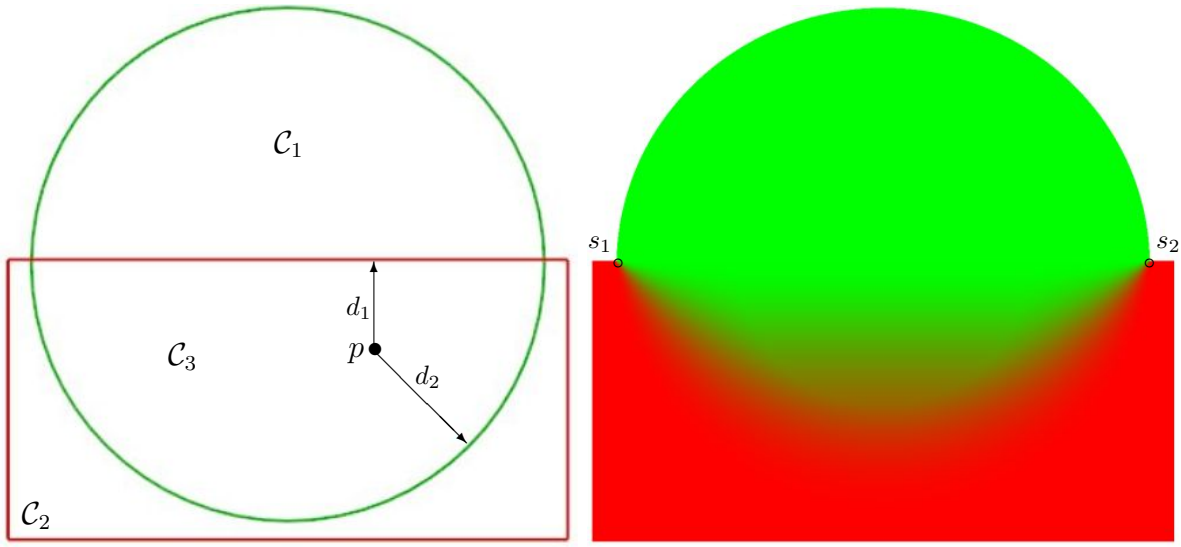

Figure 4: A planar cross section of an internal blend of materials in a V-rep union of a red box and a green cylinder. See also Figure 3.

3. VCell $\mathcal{C}_3$ as the region common to the box and the cylinder, in which we blend the materials.

Consider point $p \in \mathcal{C}_3$. The minimal distances to the boundaries of red box and the green cylinder are computed for point p, as d_1 and d_2 (see Figure 4 left). The color (material) at p will be set based on d_1 and d_2 - the smaller d_i, $i = 1, 2$ is, the closer p is to the boundary of this V-rep and hence we *diminish* its influence. Figure 4 right shows the final, smoothly blended, cross section result. This blending approach can be made arbitrary smooth by employing powers of d_i in the weighting functions, and further can be exploited even if more than two V-reps share a single VCell. See [7] for more. Then, a planar section like Figure 4 right can be used in AM, as will be shown in Section 4, as a prescription of one heterogeneous slice, allowing gradual and smooth changes between red and green materials.

Reexamine Figure 4 right. The presented blending scheme has two singular locations - where both d_1 and d_2 vanish, at points s_1 and s_2. As a result, the material is not well defined at those locations. In [32], an aim was made to handle geometry as well as material discontinuities by adding proper fillet trivariates that blend both the geometry as well as the encoded materials. See Figure 5 for an example.

Figure 6 shows a realized version of this model, 3D printed on a J55 printer of Stratasys [2]. In Section 4, we will examine how a heterogeneous V-rep model can be fabricated using 3D printing.

3.3 Trivariate and Symbolic Tools

A unique and strong capability of the GM Kernel [27] is the ability to symbolically manipulate B-spline curves, surfaces, trivariates and multivariates. All the examples mentioned in Section 2 from offsets to intersection problems [21, 2, 42], were reduced into multivariate B-spline constraints using additions, subtractions, and products of B-splines, directly in the B-spline function spaces.

[2] https://www.stratasys.com/en/3d-printers/printer-catalog/polyjet/j55-prime/ (accessed on March 2023)

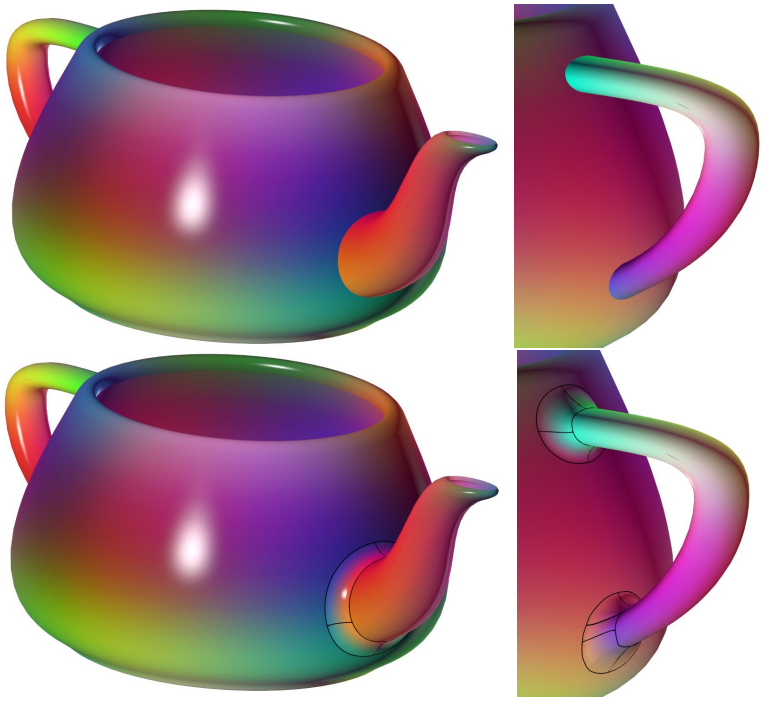

Figure 5: A graded material V-rep Utah teapot model. The C^1 discontinuities in the geometry and C^0 discontinuities in the materials (colors), at the joints between the body and the spout/handle are clear, in the top row. In the bottom row, graded heterogeneous trivariate fillets are being added, offering C^1 continuity of the geometry and C^0 in material. Note the boundaries of the fillets, in black.

Figure 6: A 3D printed graded material V-rep Utah teapot model, from Figure 5, with fillets.

This scheme, combined with the aforementioned multivariate solver, allows us to precisely compute derived geometries. Specifically, using these symbolic tools we are able to derive the functional composition [14, 12] of two spline functions. Given a parametric surface $S(u,v) : M \subset \mathbb{R}^2 \to \mathbb{R}^3$ as $S(u,v) = (s_x(u,v), s_y(u,v), s_z(u,v))$ and parametric trivariate $\mathcal{T} : D \subset \mathbb{R}^3 \to \mathbb{R}^3$ as $T(x,y,z) = (t_x(x,y,z), t_y(x,y,z), t_z(x,y,z))$ and assuming $S(u,v) \subset D$, the precise (up to machine precision) functional composition of

$$\begin{aligned} \mathcal{S}(u,v) &= \mathcal{T}(S(u,v)) \\ &= \mathcal{T}(s_x(u,v), s_y(u,v), s_z(u,v)) \end{aligned}$$

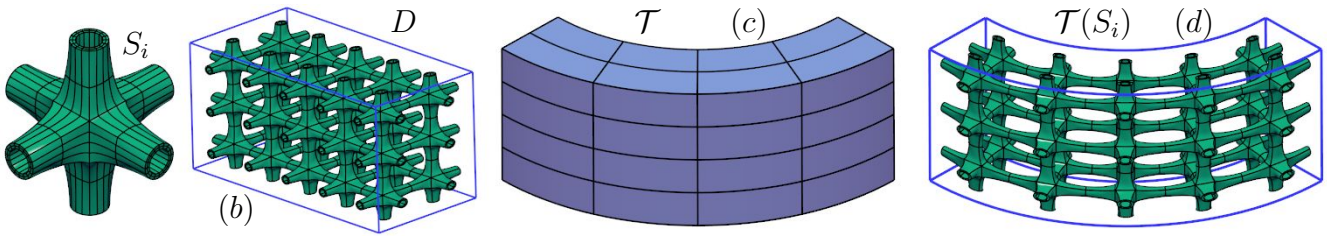

Figure 7: A simple example of functional composition. The tile in (a) consisting of over a hundred surfaces, $\{S_i\}$, is populating the domain D $(2 \times 3 \times 5)$ times, in (b), of trivariate $\mathcal{T}$, shown in (c). The result of the B-spline functional composition, $\mathcal{T}(S_i)$, is shown in (d).

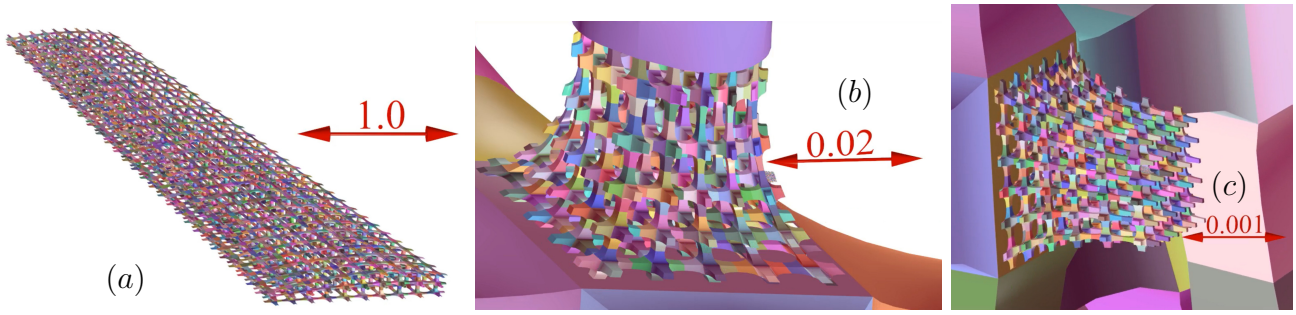

Figure 8: A multi-resolution microstructure of a wing (a), with nano-tiles (b), and pico-tiles (c). See also the movie in https://youtu.be/2wY-9fw3BMQ (accessed on March 2023).

$$
\begin{aligned}
= \; & (t_x(s_x(u,v), s_y(u,v), s_z(u,v)), \\
& t_y(s_x(u,v), s_y(u,v), s_z(u,v)), \\
& t_z(s_x(u,v), s_y(u,v), s_z(u,v))) \qquad (2)
\end{aligned}
$$

is a new surface that is mapped through $\mathcal{T}$ and into its Euclidean space. Similarly, we can compose curves into trivariate $\mathcal{T}$ or even trivariates into trivariate $\mathcal{T}$, forming a closure. Closure in the sense that the outcome is again a set of trivariates that can be further used in additional functional compositions, recursively.

The power of functional composition can be clearly portrayed with Figure 7. The *tile* in Figure 7 (a), consisting of over a hundred B-spline surfaces, $\{S_i\}$, is populating the domain D $(2\times3\times5)$ times, in (b), of trivariate $\mathcal{T}$, shown in (c). The result of the B-spline functional composition, $\mathcal{T}(S_i)$, is presented in Figure 7 (d). This result is fully conforming to the shape of $\mathcal{T}$, precisely interpolating the boundaries of $\mathcal{T}$ at the right locations, and while no tile is being clipped.

The degrees of the splines can grow quickly with additional recursive compositions. Therefore, we offer an option to employ degree reduction approximation that works extremely well when the recursive composition of a trivariate into another trivariate, yields a trivariate. Such a recursive handling can yield *multi-resolution microstructures* - we can incorporate nano-structures in the microstructures, pico-structures in the nano-structures, etc. See Figure 8 that includes snapshots captured from the movie in https://youtu.be/2wY-9fw3BMQ (accessed on March 2023).

Symbolic operations and functional composition in specific, can also be employed over higher dimensional spaces, for example when the trivariates also contain material properties. For the sake of demonstration, assume that the RGB color is our material information (as a color vector in $\mathbb{R}^3$). Heterogeneity can be encoded into the *macro-shape trivariate*, $\mathcal{T}$, as we denote the global shape of

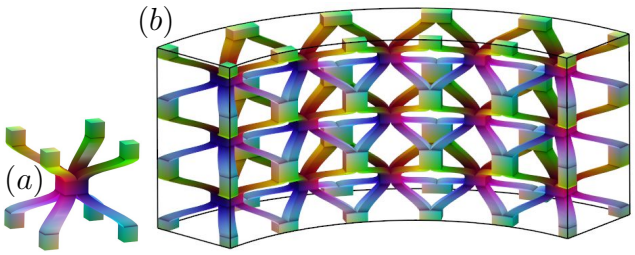

Figure 9: An example of functional composition using a heterogeneous tile (a), residing in $\mathbb{R}^6$ ($XYZRGB$). Tile (a) is composed with the same macro-shape as in Figure 7 (c), albeit from a different view, $(1 \times 3 \times 5)$ times, yielding the heterogeneous microstructure shown in (b). Note material colors are inherited in (b) from the tile (a). Compare with Figure 10.

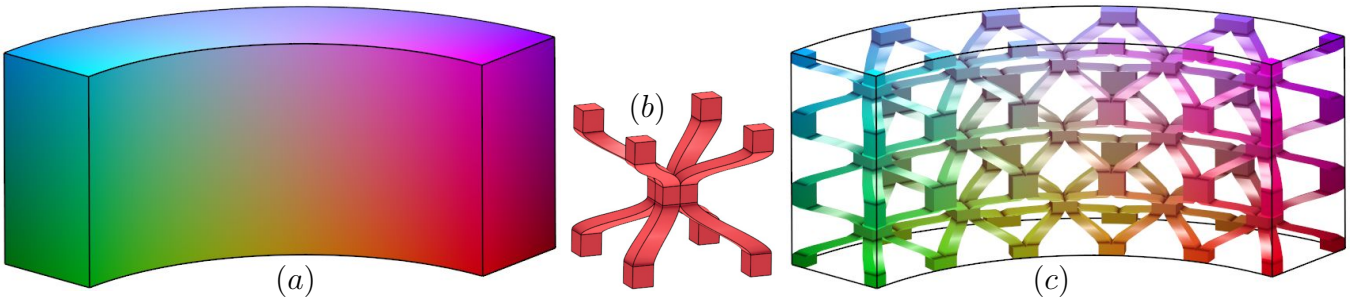

Figure 10: A simple example of functional composition using a heterogeneous macro-shape (a), residing in $\mathbb{R}^6$ ($XYZRGB$). The tile in (b) is composed $(1 \times 3 \times 5)$ times with the same macro-shape as in Figure 7 (c), heterogeneous this time, and shown from a different view in (a), yielding the heterogeneous microstructure, that is presented in (c). Note material colors are inherited in (c) from the macro-shape (a). Compare with Figure 9.

the created lattice, or, alternatively, in the tile, T, now being a set of trivariates as well. Further, the heterogeneity information can be encoded a-priori by the end user or be a result of some analysis, previously performed over the lattice.

Consider a trivariate tile T, that is in $\mathbb{R}^6$, for $XYZRGB$ or three spatial dimensions and three RGB color axes. By composing T with the macro-shape trivariate, $\mathcal{T}$, a heterogeneous microstructure can be formed. See Figure 9.

Alternatively, the macro shape trivariate, $\mathcal{T}$, can be heterogeneous in $\mathbb{R}^6$. Then, based on the positions of individual tiles in the domain of $\mathcal{T}$, D, the functionally composed result will inherit the material properties of $\mathcal{T}$. See Figure 10.

As another related direction, one can exploit the functional composition scheme toward *shell lattices*. In [11], this direction is exploited, using tiles that are derived by thickening the skeletal form of regular and semi-regular planar tiles into surfaces and trivariates. See Figure 11 for an example.

Clearly, the topic of heterogeneous, conforming to the macro-shape, microstructures is of high interest and large. More on the synthesis of heterogeneous conforming microstructures can be found in [15, 34, 22, 24].

Figure 11: A shell lattice example. Semi-regular planar B-spline tiling is used to populate the domain of a duck B-spline trivariate shell, only to yield the presented result, after functional composition.

4 Additive Manufacturing of Functionally graded Materials/Geometries

As we introduced V-reps, we have portrayed two major advantages over B-reps. One is the extensive support of (3D printing of) functionally graded materials and/or porosity and the other one is about a tight link to analysis, a topic we will briefly discuss in Section 5. In this section, we focus on additive manufacturing of heterogeneous and porous (microstructure) geometries using V-reps.

The traditional (homogeneous) 3D printing process computes parallel slices of the model-in-hand. Then, and per slice, fill commands are generated for the interior of the computed outline(s) of the intersections between the slicing plane and the VModel, that delineates the inside of the model-in-hand, from the outside.

Clearly such an approach cannot be sufficient when heterogeneity is to be supported. Some years ago, Stratasys offered a new interface to 3D printing that allows for heterogeneity and is based on a voxel representation at the proper resolution for the 3D printer. The interface is denoted *Voxel Print* [3] and it expects a stack of images instead of a stack of slices, as is traditionally done. Each image depicts one slice as before, but the different colors in the image are mapped into different materials, that in Stratasys printers can mean different colors but also translucent materials as well as the hardness of the printed materials (different Shore values) which allows for functional behavior, as will be demonstrated in the next section.

The synthesis of such a stack of images is complex. Each image (slice) is typically several thousand by several thousand pixels and we have thousands of images per model. With dozens of millions of pixels per slice, totaling many billions of pixels, the computation should be first and foremost fast. Given a VModel, one needs to identify the VCell(s) that intersect this specific slicing level z_i, and intersect each trivariate $\mathcal{T}(u,v,w) = (t_x(u,v,w), t_y(u,v,w), t_z(u,v,w))$ in each VCell with the plane $Z = z_i$ (and properly trim the geometry if so necessary). Given a specific pixel $P = (p_x, p_y)$, in image slice $Z = z_i$, this amounts to solving in $\mathcal{T}$ for (u,v,w), given,

$$\begin{aligned} t_x(u,v,w) &= p_x, \\ t_y(u,v,w) &= p_y, \\ t_z(u,v,w) &= z_i, \end{aligned} \tag{3}$$

[3] https://www.stratasys.com/en/resources/videos/voxel-the-3d-printed-pixel/ (accessed on March 2023)

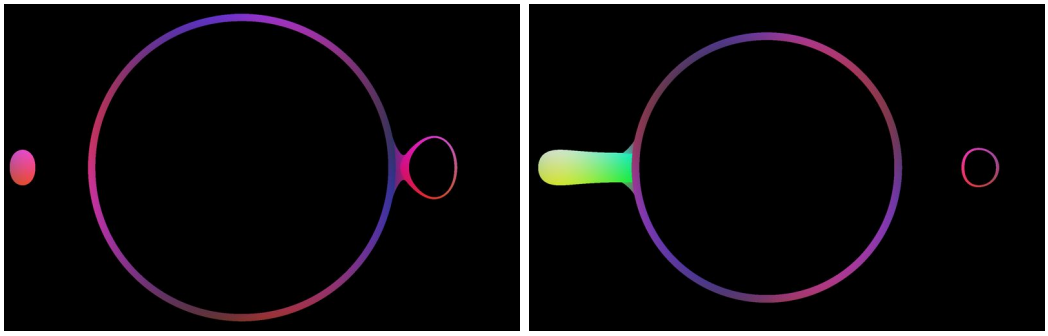

Figure 12: Two heterogeneous slices of the teapot in Figure 6. The left is at the level where the Spout is about to be detached from the body and the right at the level of the top horizontal part of the handle. Black denotes "no-material".

or three non linear equations in three unknowns. While one can employ the aforementioned multivariate solver [21, 2, 42], with many billions of pixels to solve for, such an approach is computationally infeasible, in practice. Instead, in [18], we have exploited a critical property of VModels. Given pixel P at slice $Z = z_i$, if we have a (u, v, w) solution for P, it is unique, as all VModels are constructed regular so their trivariates have positive Jacobians throughout and they do not globally intersect. In other words, all VCell(s) in the VModel have a one-to-one mapping from their domain to the Euclidean space. Exploiting this property, if we have a solution for pixel $P^{ij} = (p_x^i, p_y^j)$ in the slice, the solution to $P^{i+1,j} = (p_x^{i+1}, p_y^j)$ is going to be very similar. Hence, one can employ numerical tracing from the known solution of P^{ij}, aiming to find the solution of $P^{i+1,j}$. Knowing that the solution is unique, if we found it, we are done. This approach is highly robust and yet gains, typically, two orders of magnitudes of improvements, computationally, over the application of the full multivariate solver on all pixels in the image. Practically, only a handful of pixels in an image are computed using the full multivariate solver while the vast majority of them are robustly derived using numeric tracing. Figure 12 shows a pair of slices at different levels of the heterogeneous Utah teapot shown in Figure 6. Finally, one should recall that even with this improvement of two orders of magnitudes, it, typically, takes hours to slice a heterogeneous V-rep model.

Another 3D printing company that offers heterogeneity via a similar image-based slicing is Lithoz [4]. Here, the porosity can be controlled at the pixel level, allowing for individual pixels to contain one of two materials. Given a 3D microstructure model with a scalar density specification, this density is locally mapped to two B&W images that together approximate the relative density. Specifically, and given a V-rep model with a volumetric scalar density field, each slice of the model will be a grey-level image, grey-levels that reflect on the density. By dithering [5] the image into only black (void) or white (material) pixels, for each material, the relative density is determined.

Figure 13 exemplifies this process. In (a), a microstructure is constructed in a torus with a square cross section. Tiles in different locations hold different arms' thicknesses, while the desired material density, as prescribed by the grey-levels, varies across the model as well. Each grey-level sliced image is then dithered into two black-and-white images, as can be seen in (b) for one slice, for one (of the two) material. The final 3D printing model, after soaking it in a pink crack penetration liquid, is shown in (c). One of the two materials is more absorbent and hence such zones are more

[4] https://lithoz.com/en/ (accessed on April 2023)
[5] https://en.wikipedia.org/wiki/Dither (accessed on April 2023)

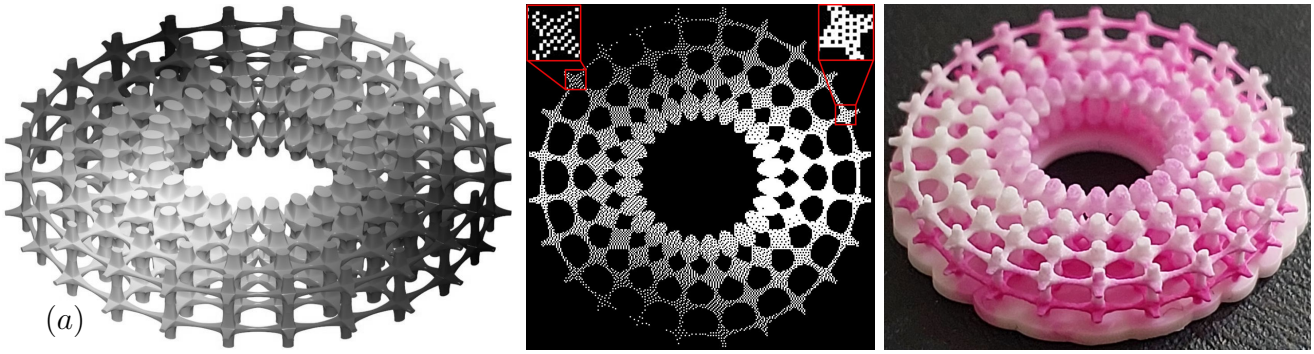

(a) (b) (c)

Figure 13: The square cross-section torus microstructure presented in (a) is heterogeneous in both the geometry of individual tiles (different thicknesses of tiles' arms at different locations) and in its tiles' porosity that is controlled via the (volumetric) grey-levels of the model in (a). (b) shows one slice of this model with the computed porosity of one of the two materials (white is material, black is void). One of the two materials here is absorbent and soaking this 3D printed model in a pink crack penetration liquid, resulted in (c). This porosity graded alumina sample (c) was fabricated by Lithoz GmbH (Vienna, Austria).

pinkish.

5 Additional Examples and Abilities

This section presents some additional V-rep examples of heterogeneous and porous geometries. All presented tangible examples were 3D printed using a J55 printer of Stratasys [6].

Different tiles in the microstructure can differ in their geometry, topology, or material content (recall Figure 9 (a)). Figure 14 shows samples of tiles of different geometries, topologies, and materials. Tiles form families, controlled by input parameters. That is, the two tiles in Figure 14 (a) are identical topologically while geometrically they differ in wall thickness and bending amounts. The two tiles in Figure 14 (c) are only similar topologically (note the two vertical bars only in one of the tiles), while also possessing different thicknesses in their different arms. The tile from Figure 9 (a) is also from the family of tiles shown in Figure 14 (c), but heterogeneous. In summary, the thicknesses of each of the arms in these tiles, as well as other geometric, topological, and material content properties are all parameters that can be set, for example, following some results of stress analysis.

For each of the six families of tiles showed in Figure 14, a pair of geometrically different shapes are shown, created via a different set of parameters within the family. In all tiles, flexible materials are drawn in green whereas in red, rigid materials are shown. Figure 14 (a) shows two variations of bistable tiles and Figure 14 (b) portrays two variations of shear/twist tiles. Figure 14 (c) presents two tiles with diagonal edges while Figure 14 (d) shows two auxetic tiles, one with a positive Poisson's ratio in all axes and one with positive/negative Poisson's ratios, in X/Y, respectively. Finally, Figure 14 (e) presents two spring tiles (of different spring coefficient) and Figure 14 (f) portrays two 3D cross tiles, one of which with a boundary surface on one face.

[6] https://www.stratasys.com/en/3d-printers/printer-catalog/polyjet/j55-prime/ (accessed on March 2023)

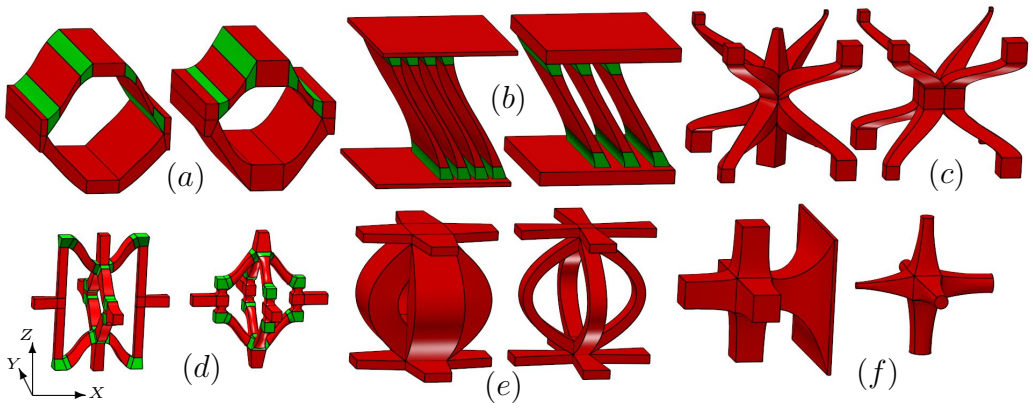

Figure 14: Different tiles that differ in their geometry (e.g., arm thicknesses), topology, and material content (different color depicts different material - in all tiles, flexible materials are drawn in green whereas in red, rigid materials are shown), while possessing different behaviors in different directions.

Most of the tiles shown in Figure 14 are employed in the rest of this section, that is organized as follows. In Section 5.1, we explore heterogeneous microstructure designs of 3D wings and in Section 5.2, heterogeneous designs of solid rocket fuel are considered. Section 5.3 examines a different application of shell lattice microstructures, that of 3D jigsaw puzzles, and in Section 5.4, we look at using the presented V-rep toward custom-made soles. In Section 5.5, two extensions are considered, of microstructures in general trimmed trivariate based V-reps and the possible use of the V-rep based microstructure synthesis to tile legacy, existing, B-rep models. Then, in Section 5.6 we consider tiling using implicit functions and finally, in Section 5.7, the use of compliant mechanism tiles is considered toward compliant microstructure mechanisms.

5.1 A Wing Model

Wings are prime candidates for lattice designs. The need for strong yet light wings is obvious. By exploiting (graded) heterogeneity, either in the geometry or materials, one can not only control the stiffness of the geometry but also adapt it to a desired shape. While analysis is not in the scope of this work, we already stated earlier that V-reps can be employed directly in iso-geometric analysis (IGA) [1]. Figure 15 shows one such example where different wings are analyzed under the same lift-load and the dihedral or wings' bending are shown for each case. The different wings differ in the geometry of individual tiles. In other words, by employing different tiles, similar to the family of tiles in Figure 14 (f), in different locations, different mechanical responses can be observed. See also the side sectional views next to each wing, in Figure 15. As a result, the three wings present three different dihedral angles, under the same lift-load.

Another wing with variations in both the geometry and material content of individual tiles is shown in Figure 16. One can observe different arm-sizes in different tiles in different locations in the wing as well as the material colors' variations that are inherited from the material prescriptions in the tiles.

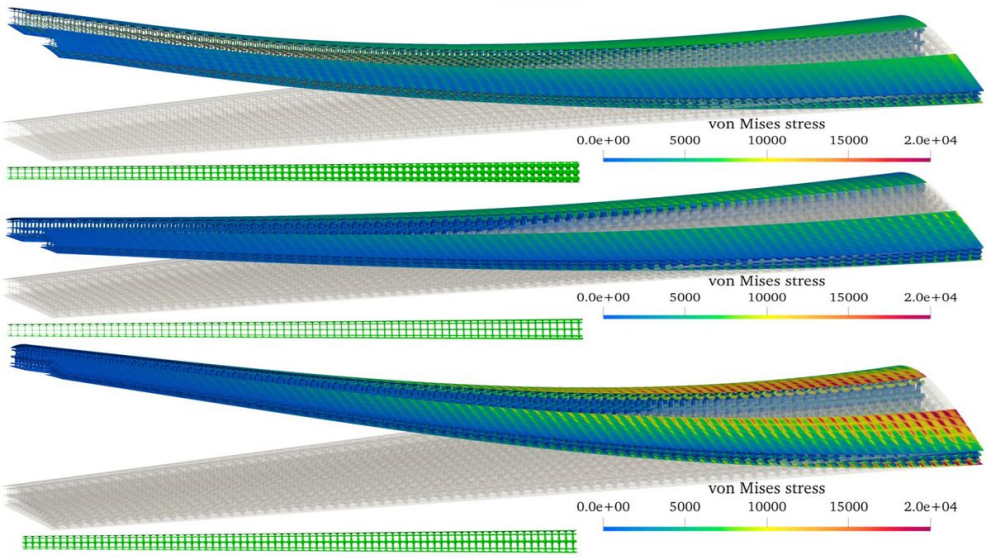

Figure 15: Iso-geometric analysis of a wing under lift load. The different dihedral bendings are due to the use of different tiles in different locations in the wing, as can be seen from the sectional views. Tiles are from the family of tiles in Figure 14 (f). Iso-geometric analysis (IGA) in collaborations with Pablo Antolin and Annalisa Buffa (EPFL Lausanne).

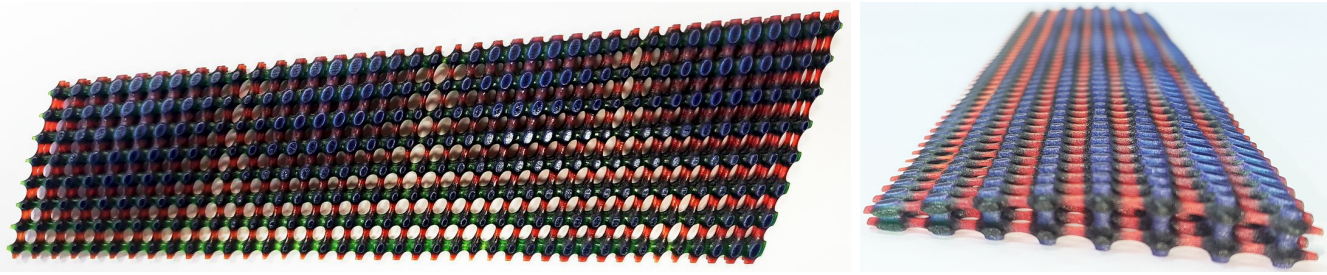

Figure 16: A 3D printed wing with (graded) heterogeneous geometry as well as (graded) materials (colors). Tiles in different locations are different geometrically as can be clearly seen via the sizes of the arms of the tiles, in different locations. Then, the tile is heterogeneous and hence all the microstructure inherits the tiles' material content. Tiles here are similar to the family of tiles in Figure 14 (f).

5.2 Heterogeneous Solid Rocket Fuel

One example where heterogeneous solids might be of great value is the application of heterogeneous solid rocket fuel (as opposed to liquid fuel). While the most challenging difficulty in this specific application is in the multi-modal analysis and optimization step, we portray how such design can be performed. Consider the example shown in Figure 17 left. Retardants in the fuel are drawn in blue and accelerants in red. The left design is aimed at an extreme boost to begin with, with accelerant concentration in the interior portions, that burns first (note the burning is occurring inside-out). The image shown in Figure 17 right exemplifies that even here graded heterogeneity with porosity can play a role while the challenges here are far greater in the analysis and in making sure all the fuel burns and does not simply break away. The potential advantage of porous solid rocket fuel is in the extremely large surface area to begin with, which can be reduced to an extreme burn, and

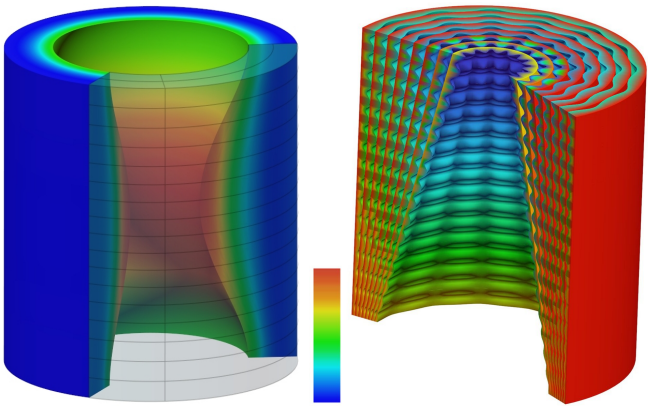

Figure 17: Two variants of solid rocket fuel, as trivariate(s) heterogeneous fuel with accelerants (in red) and retardants (in blue), are presented. The scale presents the relative gradient from maximal amount of accelerants (in red) to maximal amount of retardants (in blue), in the fuel. The right example shows that even here heterogeneity with porosity can play a role.

hence boost, in a very short time. Interestingly enough, 3D printing of solid rocket fuel is already under active research [7].

5.3 A 3D Jigsaw Puzzle

In Figure 11, we show that one can employ V-reps toward general shell freeform lattices. In [16], we have used this scheme with tiles that are jigsaw puzzles based. By randomly yet smoothly perturbing the puzzle tiles a bit and mapping them, using functional composition, over general V-rep shell models, a 3D jigsaw puzzle can be created, with all tiles being different. Figure 18 shows one example of a 3D printed model of a jigsaw puzzle created for a V-rep model of the Utah teapot.

5.4 Shoe/in-soles

In recent years, 3D printing of soles has been attempted by many, including commercially [8]. While heterogeneity in either the material content or geometry has been rarely examined, not to say graded heterogeneity, we attempted exactly that. The sole in Figure 19 is custom made to a specific 3D scan, and once the geometry of the customed sole is reconstructed as a trivariate, a conforming microstructure is automatically created for it, using functional composition. Also of interest, is the fact that the sole is functionally graded material-wise. The front (in black) is flexible and gradually becomes rigid toward the back (in grey). One can envision 3D printing such custom made soles, where the sole is only soft in locations with ulcers, an unfortunately common phenomena in diabetic persons, for example.

[7] https://aerospaceamerica.aiaa.org/departments/3d-printed-rocket-fuel (accessed on March 2023)

[8] See, for example: https://www.eos.info/en/all-3d-printing-applications/people-health/sports-lifestyle-consumer-goods/shoes-soles and https://www.materialise.com/en/inspiration/cases/adidas-futurecraft-3d-printed-personalized-shoe (accessed on March 2023).

Figure 18: A 3D printed jigsaw puzzle of the Utah teapot, as a shell microstructure. Top to bottom, shown are the 3D computer model, the different 3D printed puzzle pieces, partial assembly of the model and the final result.

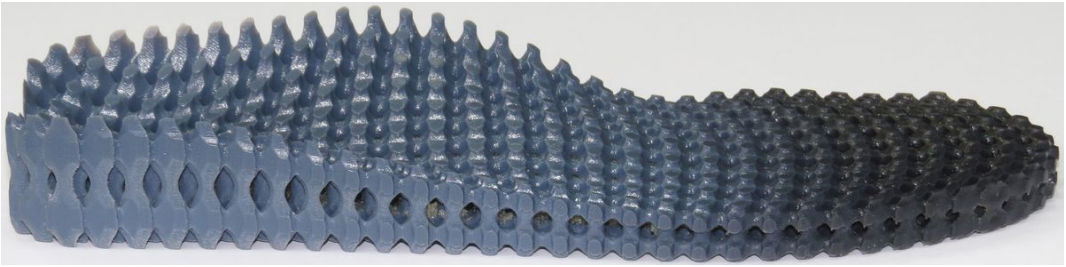

Figure 19: A 3D printed heterogeneous microstructure of a shoe sole. The front of the sole (in black) is flexible while the back size (in grey) is more rigid. Note the gradual change between the black and grey materials. Tiles from the family in Figure 14 (f).

5.5 Microstructures in Trimmed V-reps and general B-reps

Most of the presented models so far exploited a single macro-shape trivariate. However, given a full VModel, consisting of several (trimmed) trivariate VCells, as a result of Boolean operations, one can populate the valid regions in all trimmed trivariates with the proper tiles, only to build bridging tiles between adjacent VCells. This process is demonstrated in Figure 20, where a hole is subtracted from a body of duck (similar to Figure 11) near the tail, only to be united with the two wings, forming three primary VCells - for the body with the tail hole and the two wings, and two additional VCells in the common zone between the body and each of the wings. The yellow tiles in Figure 20 are tiles in the body with neighboring tiles that were partially or fully trimmed and hence purged away. In other words, the yellow tiles in the body are those next to the common zones. Then, red bridging tiles are built to link together the adjacent microstructures (yellow in the body), in the primary VCells. See [22] for more.

All we have presented until now was based on a macro-shape that is a trivariate V-rep. However, considering the huge set of legacy B-rep models, it is also desirable to aim at populating (almost) conforming microstructures, in general B-rep models. Following the similar ideas we just presented, for general trimmed V-rep models, we allow the population of general B-rep models, with microstructures, via an auxiliary 3D field that is defined to capture the general shape of the B-rep model. This, in a similar way to the use of cages in computer graphics, for deformation [6]. Herein, the auxiliary field is defined as a trivariate cage that governs the placement of the individual tiles. Tiles that are found to be on the boundary or outside the B-rep, are purged only to build precise bridging tiles from their neighbors to the B-rep. Figure 21 presents one example using the Stanford bunny - a polygonal B-rep model. In Figure 21 (a), the Stanford bunny is shown in a white transparent color. The trivariate cage built for it is also shown in red wire-frame colors. Interestingly, herein, the trivariate cage has a C^0 discontinuity and it splits near the ears, while it is still supported as a macro-shape in the functional composition. Finally, (a) also shows the tiles built using the cage and are found inside the bunny. Green tiles are interior ones, yellow tiles are next to the boundary and blue tiles are bridging tiles from the yellow tiles and the boundary of the bunny. Figure 21 (b) shows the microstructure with graded colors encoded, whereas (c) presented a 3D printed version with the microstructure embedded in the bunny that is printed in a translucent material. See [24] for more.

The continuity of the resulting functional composition, $\mathcal{T}(S)$ (recall Equation (2)), is governed by the lower continuity between $\mathcal{T}$ and S. In Figure 21, the macro-shape trivariate $\mathcal{T}$ has a

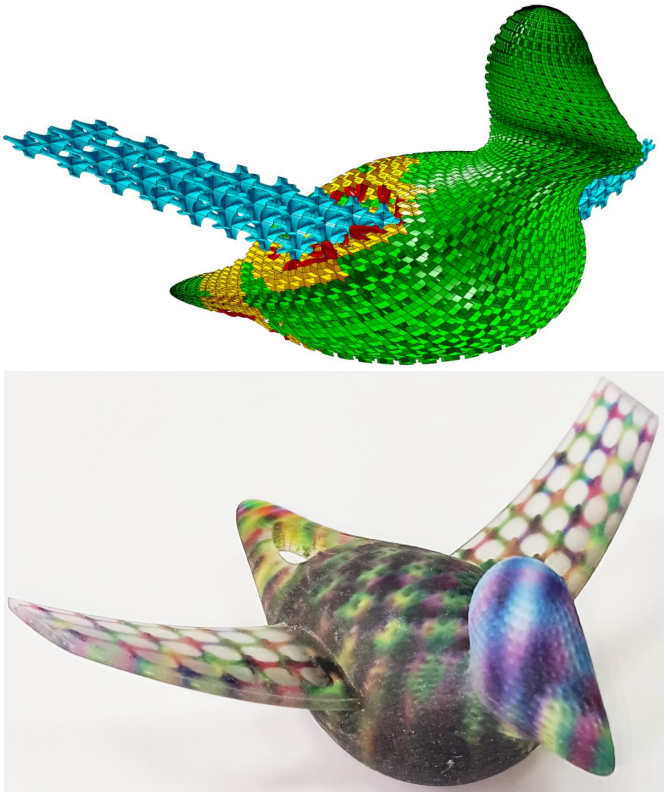

Figure 20: A 3D printed heterogeneous microstructures of a trimmed V-rep model of a duck with wings. Note the tail is also trimmed. Top shows the full microstructure with red tiles serving as bridging tiles and yellow tiles are adjacent to them, in the body. The 3D printed model is shown at the bottom with the microstructure embedded in the full trimmed V-rep model, 3D printing using a translucent material. Tiles from the family in Figure 14 (f).

C^0 discontinuity split, due to the ears. Yet, we managed to build a microstructure through it by carefully positioning the tiles in the domain of the macro-shape, so they will never cross this discontinuity. In general, every time a tile crosses a knot plane in the domain of $\mathcal{T}$ (that induces some finite continuity), the composed tile will also lose continuity along that knot plane. In [43], several remedies for this challenge are presented.

5.6 Implicit Tiling

Contemporary GM systems support other representations beyond NURBs based B-reps. Implicit (trigonometric in specific) functions and polygonal meshes are, to a certain extent, also supported in some GM systems. Interestingly, even the original FFD work [40] can be employed to approximate the functional compositions of polygonal meshes. That said, the challenges in the (evaluation of) composition of implicit function are significant and in this section, we focus on the latter - functional composition and construction of microstructures using implicit tiles.

Recall Section 3.3, but now the tile will be a scalar (implicit) trivariate $\mathcal{I}(x, y, z) : [0, 1]^3 \rightarrow \mathbb{R}$. $\mathcal{I} > 0$ will denote the interior of the tile, and $\mathcal{I} = 0$ its boundary. Like the parametric tiles in Section 3.3, $\mathcal{I}$ will typically be periodic.

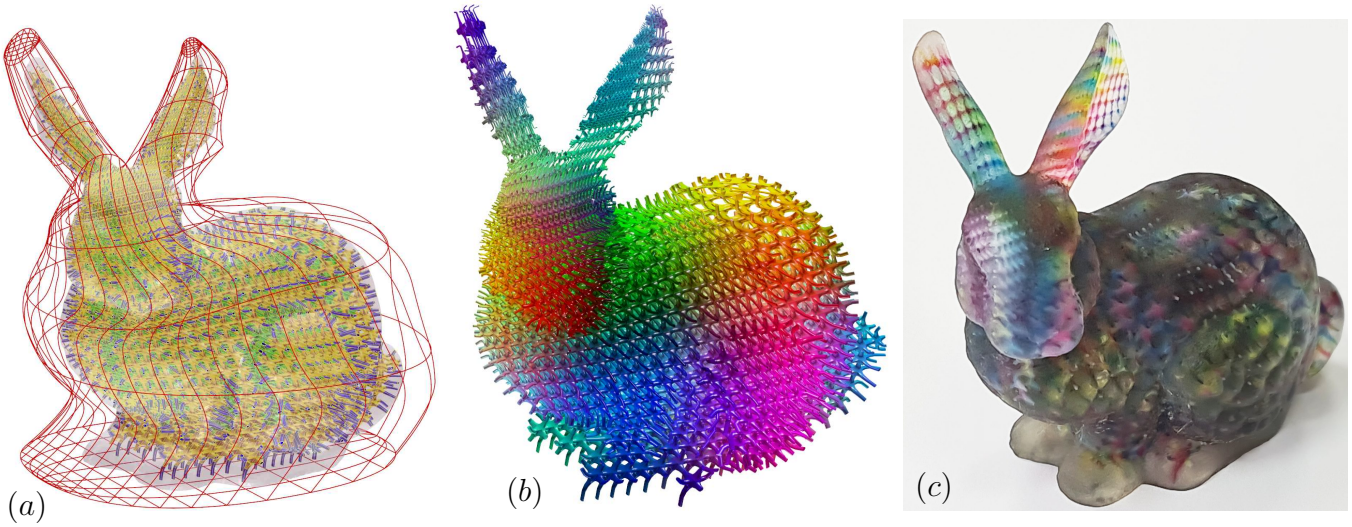

Figure 21: A 3D printed heterogeneous microstructures embedded in a polygonal B-rep model of the Stanford bunny. (a) shows the Stanford bunny transparent with the trivariate cage (in wire-frame red) created for it. Also shown in (a) are the tiles that are found inside the bunny, in green, the bridging tiles to the boundary, in blue, and the bridged tiles, in yellow. In (b), the full microstructure model is shown in graded heterogeneous colors, and (c) presents a colored 3D printed result, embedded in the original B-rep model, 3D printed in a translucent material. Tiles from the family in Figure 14 (f).

Denote the implicit surface of $\mathcal{I} = 0$ as S_0. Then, and as before, S_0 can be mapped through the macro-shape $\mathcal{T}(u, v, w)$ to the Euclidean space, as $\mathcal{T}(S_0)$. Some previous work on implicit microstructures (i.e. [25]) exploited this direction, and by providing a piecewise linear approximation of S_0, a polygonal approximation of the entire microstructure geometry can result. Interesting and due to the huge polygonal data set that might result, a procedural representation was also proposed in [25] to alleviate this data-explosion difficulty.

Nonetheless and beyond the data-size difficulty, the use of a polygonal approximation of implicits also introduces errors that can be further augmented by the mapping through the macro-shape, $\mathcal{T}$. In [23], we offer an alternative to processing implicit tiling that is arbitrarily precise, a process that is similar to the solution we employed for parametric forms (Recall Equation (3)).

Given a specific location (x_i, y_i) in a slicing level z, we need to identify if $\mathcal{T}$ contains this location, and if so the solution parameters (u, v, w). Hence, we solve for (u, v, w) in:

$$\begin{aligned} \mathcal{T}_x(u, v, w) &= x_i, \\ \mathcal{T}_y(u, v, w) &= y_i, \\ \mathcal{T}_z(u, v, w) &= z, \end{aligned} \tag{4}$$

using our multivariate constraints solver [21]. If the location is found outside $\mathcal{T}$ (no solution), we stop. Otherwise, and because all the domain of $\mathcal{T}$ is populated with a 3D grid of implicit tiles, we locate the implicit tile $\mathcal{I}$ that holds that (u, v, w) location in $\mathcal{T}$. Let $(\overline{u}, \overline{v}, \overline{w})$ be the affinely mapped (u, v, w) location to the domain of $\mathcal{I}$. Then, by evaluating the implicit we precisely determine if this location is inside the microstructure model ($\mathcal{I}(\overline{u}, \overline{v}, \overline{w}) > 0$) or not. The same numeric tracing optimization we applied for parametric tiles in Section 4 can be used here as well, achieving a robust

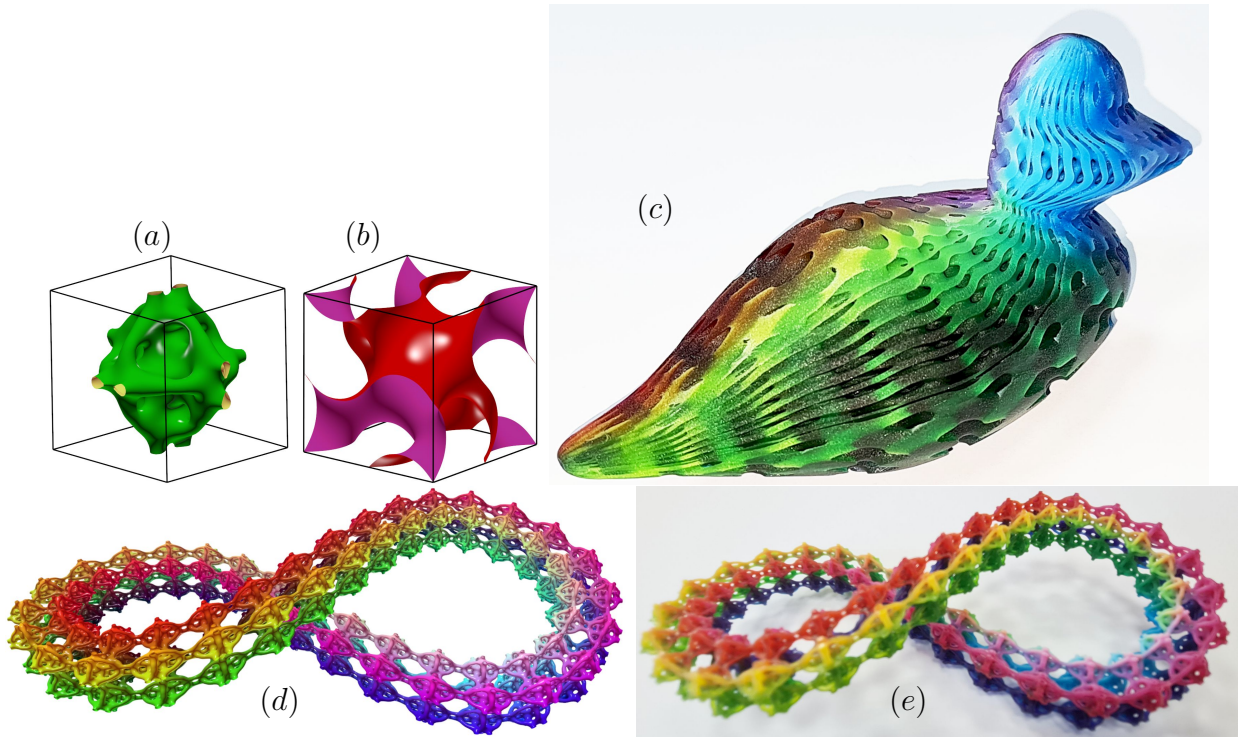

Figure 22: 3D microstructures formed using implicit tiles. In (a), a general implicit trivariate tile shape is shown and in (b) a (trigonometric) Gyroid. (c) shows a 3D printed duck microstructure with the implicit Gyroid tile (b) whereas (d) shows a 3D computer model and (e) shows a 3D printed model of an infinity shape with the implicit tile in (a).

yet efficient evaluation of the entire image-slide.

By evaluating individual (pixel) locations in the implicits we have not only gained arbitrary precision (up to the desired slicing image resolution), but we also achieved an ability to support heterogeneity. $\mathcal{I}$ can now be $\mathcal{I}(x, y, z) : [0, 1]^3 \rightarrow \mathbb{R}^k,\ k > 1$ where, for $k > 1$, one can hold material properties. Having the (u, v, w) solution from Equation (4), this merely means the evaluation of $\mathcal{I}$ and extracting the material at location (x_i, y_i, z) from the $k > 1$ coordinates of $\mathcal{I}$. Alternatively, material information can be deduced from the macro-shape $\mathcal{T}$, following Equation (1).

Figure 22 shows two examples of heterogeneous microstructures that were created and 3D printed using implicit tiles. The heterogeneous properties (color) in both cases were inherited from the macro-shape. See [23] for more on Microstructure with implicit tiles.

5.7 Compliant Microstructure Mechanisms

One powerful ability of building microstructures using functional composition is the fact that no tile is being clipped. Because all tiles are fully preserved topologically and the geometric deformation (in the local) of individual tiles is minimal, one can employ functional tiles, possibly with varying behavior, in a microstructure based on a macro-shape V-rep. In other words, if a tile behaves as a (compliant) mechanism, it will preserve its functionality after the functional composition or the mapping into Euclidean space. This, unlike the common practice of clipping tiles, that are

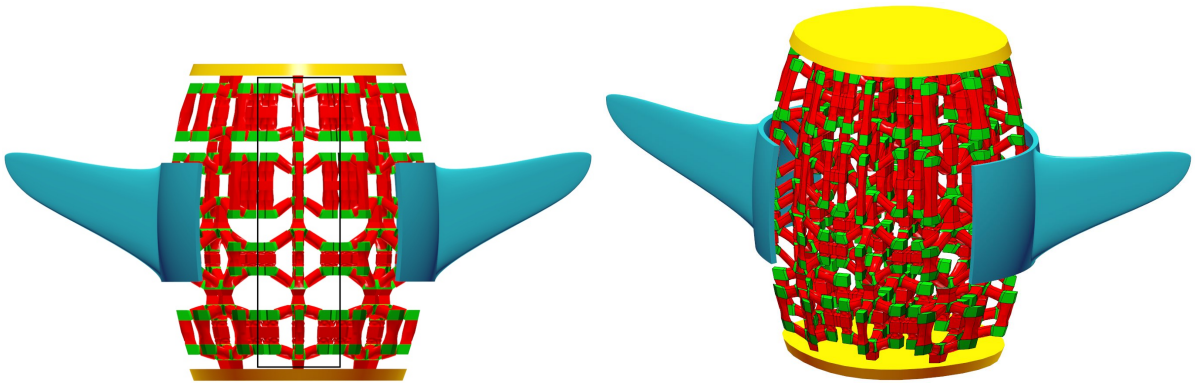

Figure 23: A 3D printed heterogeneous compliant mechanism microstructure, consisting of different 3D auxetic tiles. Note the black rectangle on the left that highlight the different auxetic tiles. See also the movie in https://youtu.be/NKck4N7TKQI (accessed on March 2023) for the vertical force response. Tiles from the family in Figure 14 (d).

positioned in a 3D axes parallel grid, to the freeform shape in hand. As a result, tiles on the boundaries are typically truncated, and hence likely to lose their functioning abilities.

We present three such examples. Consider a microstructure consisting of auxetic tiles (recall Figure 14 (d)). By embedding different tiles in different locations in the microstructure, a vertical pressure will yield an arbitrary shrinking or expanding response, and as desired, in X and Y. In Figure 23, a barrel-like macro-shape trivariate V-rep is populated with different auxetic tiles. Recall that flexible materials are drawn in green whereas in red, rigid materials are shown. Note the column of tiles, marked with a black rectangle, in Figure 23 left. All the auxetic tiles along this column are different. As a result, a vertical pressure will cause some tiles to shrink in X and Y and some to expand. See the movie in https://youtu.be/NKck4N7TKQI (accessed on March 2023) for the pressure response and the resulting motion of the two wings.

Our second example is using the shear/twist tiles (recall Figure 14 (b)), that twists to one side when a vertical pressure is applied. Figure 24 left presents a (piecewise linear) tubical trivariate V-rep, in a translucent color, populated with a twist tile (all tiles are the same here). Here again, flexible materials are drawn in green whereas in red, rigid materials are shown. The final model, with caps and wings to visually augment the twisting effect, is shown in Figure 24 right. See the movie in https://youtu.be/c3QUUFxBOyI (accessed on March 2023) for the pressure response in this case.

Our third example is using the bistable tiles (recall Figure 14 (a)), that can assume two stable states. The states shown in Figure 14 (a) are the expanded state in which the geometry is also 3D printed and designed. Yet, and due to flexibility of the top arms in this tile, it can also collapse to a much smaller state as can be seen in the movie in https://youtu.be/JTqGKculxgc (accessed on March 2023). The computer model, is shown in Figure 25 (a), the 3D printed model in (b), and the 3D printed model in a collapsed state is shown in (c).

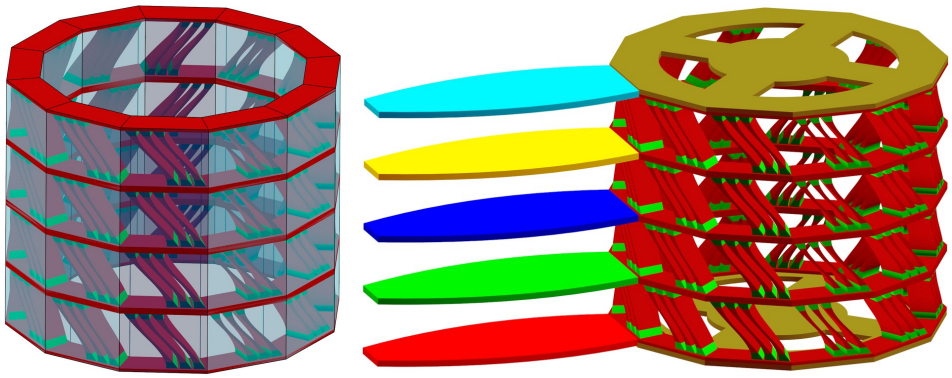

Figure 24: A twisting 3D printed heterogeneous compliant mechanism microstructure. See also the movie in https://youtu.be/c3QUUFxBOyI (accessed on March 2023) for the vertical force response. Tiles from the family in Figure 14 (b).

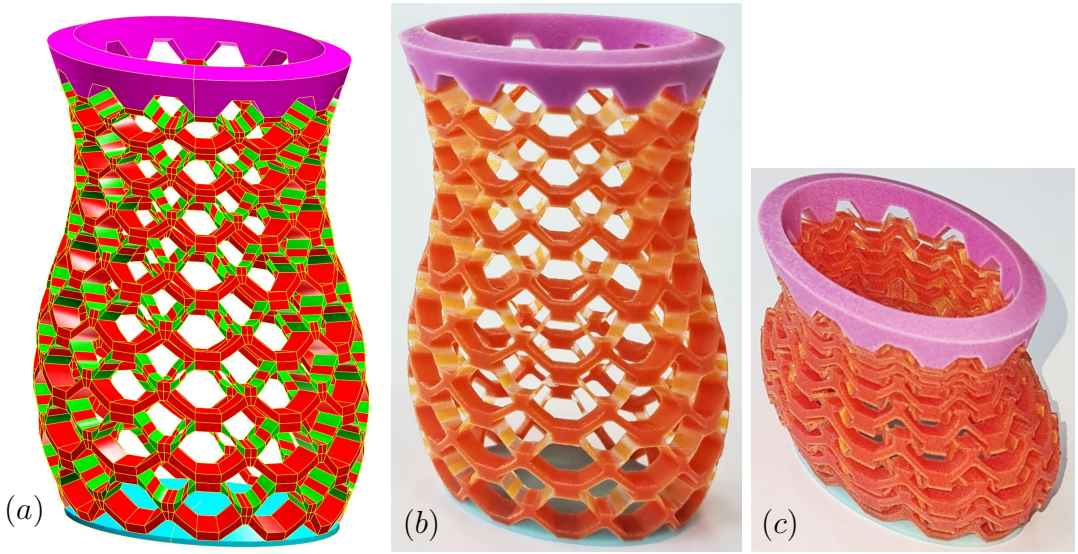

Figure 25: A bistable vase. This microstructure, in the shape of an ovalic vase, can be collapsed to about 50% of its original height. The computer model is shown in (a), the 3D printed version in (b) and the collapsed state of the 3D printed model is shown in (c). See also the movie in https://youtu.be/JTqGKculxgc (accessed on March 2023) for this bistable behavior. Tiles from the family in Figure 14 (a).

6 Conclusions and the Future of V-reps

In this work, we have reviewed a decade of development using V-reps and volumetric B-spline based representations, mostly in the context of additive manufacturing. The advantages over traditional B-reps are significant - extensive control over microstructures' design and full support of graded heterogeneity, two much needed abilities in additive manufacturing today, abilities that are lagging behind in contemporary B-rep based GM systems.

Further, the connections between the design stages and the analysis/optimization stages are much tighter with V-reps, compared to B-reps, as no conversions between function spaces is now required. Beyond the immediate compatibility with iso-geometric analysis [29, 10], the ability to

synthesize classic 3D finite element meshes, when a volumetric parametrization is in hand, is much simplified.

The modeling processes using V-reps, from the end-user perspective, are similar to B-rep based modeling, as was discussed here: Volumetric primitive can be prescribed, in the end-user interface, in a similar way to B-rep primitives in contemporary GM systems, and same for high level constructors such as sweeps, rulings, and extrusions. The complexity of performing Boolean operations in V-rep is similar to that of B-reps, with the added complexity of handling heterogeneous properties, as well as blending them. The effort of building a whole new GM system is huge, and is not clear if V-reps should completely replace B-reps as the internal representation of choice in GM systems or simply augment existing GM systems with V-rep abilities, with the realization that the boundaries of V-reps are B-reps.

That said, B-reps suffers from additional deficiencies. As discussed in Section 3.2, doing Boolean operations on highly complex B-rep geometries, like in Figures 19 or 20, is a challenge even in the state-of-the-art B-reps systems. Since the boundaries of our V-reps are merely B-reps, this difficulty should still be addressed, for B-reps as well as V-reps.

As stated in Section 5.6, implicits are also employed in modern GM and triply periodic minimal surface (TPMS) tiles, such as Gyroids, are commonly exploited. While there are evidence on the use of Gyroids-similar geometry in nature (i.e. [35]), the optimality of those tiles, like any other tile's shape and/or topology is clearly application dependent and should be further investigated. Very little can be said on the optimality of these implicits or other tiles.

Specifically, one should recall not only that TPMS geometry is typically approximated, but the tiles undergo some small yet not insignificant deformations by the mapping through the macro-shape. Building the microstructure, as is done herein and also, for example in [25], the geometry after the mapping is no longer preserving the zero mean curvature (minimal surface) property.

The presented functional composition based microstructures allows the separation of the design problem into two: the design of the macro-shape and the design of micro-tile(s). Optimization can now be applied to those two problems, with some levels of independence. Tiles' shapes (as well as their material and topology) should be globally and a-priori analyzed and optimized, for any expected physical task. For example, via topological optimization (TO) [3] that has captured a leading place as a solution for achieving optimal geometry and topology (and material distribution), for some task in hand. Then, a parametric family of optimized tiles for the given task can be constructed once and employed for specific optimization tasks, for example, to control the dihedral angle of a wing, as in Figure 15. Furthermore, in this work we portrayed solution to precisely handling implicit tiling. Interestingly, one can already find some work on iso-geometric analysis (IGA) of implicits, for example [39].

When tiles vary in their shape and material content throughout the macro-shape, the aim should be to preserve any needed continuity of both the shape and the material content, between all neighboring tiles in the macro-shape. By having tiles that can present different geometry and material content on their different boundaries, the desired continuity can be achieved. For parametric form, this was done, for example, for the wing in Figure 16. Desired continuity can be also be achieved for implicit forms, with varying geometry, as was done in [23] using implicit tiles that were represented using trivariate functions, as in Figure 22 (a). Yet, achieving, for example, arbitrarily continuous yet gradual control over wall-thicknesses and/or material changes in Gyroid tiles is a more challenging task.

For the most part, the presented work was exploiting tiles that were organized in the macro-

shape as cubes, topologically. Nevertheless, many other schemes, regular, semi-regular, general and even a-periodic methods to tile the plane and 3-space exist and clearly some can posses superior properties (consider the shape of a honey-comb). Such approaches to synthesize individual tiles and tile the 2/3-space should be examined in this microstructures context.

All those microstructures are highly repetitive and parallelism of algorithms can be greatly beneficial, computationally. For example the slicing of the model in [23] was parallelized with an immediate boost that was almost inverse proportion to the number of used processors.

Needless to say, additive manufacturing is an enabling technology for heterogeneity and porosity. Many other applications await further research here, beyond what was presented in this work, such as heat exchangers and controlled heat transfer [44], aero-space applications, food, implants and other medical applications, batteries, protective gears, etc. Only time will tell how far could we all advance these and other fields.

Finally, all presented algorithms and tools are freely available, for non-academic use, in C/C++ source code level, in [27]. A end-user graphical user interface for this kernel is also available in https://csaws.cs.technion.ac.il/∼gershon/GuIrit (accessed on March 2023).

7 Acknowledgments

This project has received funding from the European Union Horizon 2020 research and innovation programme, under grant agreement No 862025, was supported in part by the ISRAEL SCIENCE FOUNDATION (grant No. 597/18) and with funding from the Defense Advanced Research Projects Agency (DARPA), under contract HR0011-17-2-0028. The views, opinions and/or findings expressed are those of the author and should not be interpreted as representing the official views or policies of the Department of Defense or the U.S. Government.

The author would like to thank the reviewers of this work for their valuable comments and for raising very interesting questions that helped to greatly improve this work.

References

[1] Antolin, P., Buffa, A., and Martinelli, M. Isogeometric analysis on v-reps: First results. *Computer Methods in Applied Mechanics and Engineering 355* (2019), 976–1002.

[2] Bartoň, M., Elber, G., and Hanniel, I. Topologically guaranteed univariate solutions of underconstrained polynomial systems via no-loop and single-component tests. *Computer-Aided Design 43*, 8 (2011), 1035–1044.

[3] Bendsoe, M. P., and Sigmund, O. *Topology Optimization*. Springer, 2002.

[4] Bezier, P. General distortion of an ensemble of biparametric patches. *Computer Aided Design 10* (1978), 116–120.

[5] Borden, M., Scott, M., Evans, J., and Hughes, T. Isogeometric finite element data structures based on bezier extraction of nurbs. *Internat. J. Numer. Methods Engrg. 87* (2011), 15–47.

[6] Chen, L., Huang, J., Sun, H., and Bao, H. Technical section: Cage-based deformation transfer. *Comput. Graph. 34*, 2 (Apr 2010), 107–118.

[7] Cirillo, E., and Elber, G. Handling heterogeneous structures and materials using blending schemes in v-reps. *Computer Aided Geometric Design 83* (2020), 101942.

[8] Cobb, J. E. Tiling the sphere with rational bézier patches. In *Report TR UUCS-88-009*. University of Utah, USA, 1988.

[9] Conkey, J., and Joy, K. Using isosurface methods for visualizing the envelope of a swept trivariate solid. *UC Davis: Institute for Data Analysis and Visualization* (2000).

[10] Cottrell, J. A., Hughes, T. J., and Bazilevs, Y. *Isogeometric analysis: toward integration of CAD and FEA*. John Wiley & Sons, 2009.

[11] Dahiya, S., Shein, A., and Elber, G. Shell-lattice construction based on regular and semi-regular tiling via functional composition. In *The Hyperseeing magazine* (2021), vol. Fall 2021, pp. 12–23.

[12] DeRose, T. D., Goldman, R. N., Hagen, H., and Mann, S. Functional composition algorithms via blossoming. *ACM Trans. Graph. 12*, 2 (Apr. 1993), 113–135.

[13] Dokken, T., Skytt, V., and Barrowclough, O. Trivariate spline representations for computer aided design and additive manufacturing. *Computers & Mathematics with Applications 78*, 7 (2019), 2168–2182. Simulation for Additive Manufacturing.

[14] Elber, G. *Free Form Surface Analysis Using A Hybrid of Symbolic and Numerical Computation*. PhD thesis, University of Utah, 1992.

[15] Elber, G. Precise construction of micro-structures and porous geometry via functional composition. In *International conference on mathematical methods for curves and surfaces* (2016), Springer, pp. 108–125.

[16] Elber, G., and Kim, M.-S. Synthesis of 3d jigsaw puzzles over freeform 2-manifolds. *Computers & Graphics 102* (2022), 339–348.

[17] Elber, G., Kim, Y.-J., and Kim, M.-S. Volumetric boolean sum. *Computer Aided Geometric Design 29*, 7 (2012), 532 – 540. Geometric Modeling and Processing 2012.

[18] Ezair, B., Dikovsky, D., and Elber, G. Fabricating functionally graded material objects using trimmed trivariate volumetric representations. In *Proceedings of SMI'2017 Fabrication and Sculpting Event (FASE)* (2017).

[19] Feng, J., Nishita, T., Jin, X., and Peng, Q. B-spline free-form deformation of polygonal object as trimmed bezier surfaces. *The Visual Computer 18* (2002), 493–510.

[20] Ferguson, J. Multivariable curve interpolation. *J ACM 11* (1964), 221–228.

[21] Hanniel, I., and Elber, G. Subdivision termination criteria in subdivision multivariate solvers using dual hyperplanes representations. *Computer-Aided Design 39*, 5 (2007), 369–378.

[22] Hong, Q. Y., and Elber, G. Conformal microstructure synthesis in trimmed trivariate based v-reps. *Computer-Aided Design 140* (2021), 103085.

[23] Hong, Q. Y., Elber, G., and Kim, M. S. Implicit functionally graded conforming microstructures. *Computer-Aided Design 162* (2023), 103548.

[24] Hong, Q. Y., Park, Y., and Elber, G. Conformal parametric microstructure synthesis for boundary representations. *The Hyperseeing magazine* (2022).

[25] Hu, C., and Lin, H. Heterogeneous porous scaffold generation using trivariate b-spline solids and triply periodic minimal surfaces. *Graphical Models 115* (2021), 101105.

[26] Hu, S.-M., Zhang, H., Tai, C.-L., and Sun, J.-G. Direct manipulation of ffd: efficient explicit solutions and decomposible multiple point constraints. *The Visual Computer 18* (2001), 370–379.

[27] Irit. The irit geometric modeling environment, version 12., 2023. https://csaws.cs.technion.ac.il/∼gershon/irit.

[28] Joy, K., and Duchaineau, M. A. Boundry determination for trivariate solids. In *Proceedings of the 1999 Pacific Graphics Conference* (1999), pp. 82–91.

[29] Kagan, P., Fischer, A., and Bar-Yoseph, P. Mechanically based design: adaptive refinement for b-spline finite element. In *Proceedings International Conference on Shape Modeling and Applications* (2001), IEEE, pp. 345–366.

[30] Mantyla, M. *An Introduction to Solid Modeling*. Computer Science Press, 1988.

[31] Martin, T., Cohen, E., and Kirby, R. Volumetric parameterization and trivariate b-spline fitting using harmonic functions. *Computer Aided Geometric Design 26*, 6 (2009), 648–664. Solid and Physical Modeling 2008.

[32] Masalha, R., Cirillo, E., and Elber, G. Heterogeneous parametric trivariate fillets. *Computer Aided Geometric Design 86* (2021), 101970.

[33] Massarwi, F., and Elber, G. A b-spline based framework for volumetric object modeling. *Computer-Aided Design 78* (2016), 36–47. SPM 2016.

[34] Massarwi, F., Machchhar, J., Antolin, P., and Elber, G. Hierarchical, random and bifurcation tiling with heterogeneity in micro-structures construction via functional composition. *Computer-Aided Design 102* (2018), 148–159.

[35] Michielsen, K., and Stavenga, D. G. Gyroid cuticular structures in butterfly wing scales: biological photonic crystals. *J. R. Soc. Interface 5* (2008), 85–94.

[36] Peltier, S., Morin, G., and Aholou, D. Tubular parametric volume objects: Thickening a piecewise smooth 3d stick figure. *Computer Aided Geometric Design 85* (2021), 101981.

[37] Pimpalkar, A., Agrawal, V., and Gautam, S. Trivariate model construction from b-rep nurbs geometries for isogeometric analysis. *Recent Advances in Computational and Experimental Mechanics, Vol I. Lecture Notes in Mechanical Engineering. Springer, Singapore* (2022), 459–471.

[38] Raviv, A., and Elber, G. Interactive Direct Rendering of Trivariate B-Spline Scalar Functions. *IEEE Transactions on Visualization and Computer Graphics 7* (2001), 109–119.

[39] Saye, R. I. High-order quadrature methods for implicitly defined surfaces and volumes in hyperrectangles. *SIAM Journal on Scientific Computing 37*, 2 (2015), A993–A1019.

[40] Sederberg, T. W., and Parry, S. R. Free-form deformation of solid geometric models. *SIGGRAPH Comput. Graph. 20*, 4 (aug 1986), 151–160.

[41] Song, Y., and Cohen, E. Making trimmed b-spline b-reps watertight with a hybrid representation. In *International Design Engineering Technical Conferences and Computers and Information in Engineering Conference* (08 2019), vol. Volume 2B: 45th Design Automation Conference.

[42] van Sosin, B., and Elber, G. Solving piecewise polynomial constraint systems with decomposition and a subdivision-based solver. In *Computer Aided Design* (2017), vol. 90, pp. 37–47.

[43] van Sosin, B., and Elber, G. Crossing knot lines in composition of freeform b-spline geometry. *Computer Aided Geometric Design 62* (2018), 217–227.

[44] Zwar, J., Elber, G., and Elgeti, S. Shape optimization for temperature regulation in extrusion dies. *The Journal of Mechanical Design 145*, 1 (2023), 012004.